

# Identification of natural frequencies of Pelton runners during transient operating conditions

M. Chiarelli<sup>1</sup>, R. M. Boes<sup>2</sup>, D. F. Vetsch<sup>2</sup>, G. Blommaert<sup>3</sup>, M. Boden<sup>4</sup>, C. Münch-Alligné<sup>1</sup>

<sup>1</sup> Institute of Systems Engineering, School of Engineering, HES-SO Valais-Wallis,  
Rue de l'Industrie 23, CH-1950, Sion, Switzerland

<sup>2</sup> Laboratory of Hydraulics, Hydrology and Glaciology (VAW), ETH Zurich,  
Hönggerbergring 26, CH-8093, Zurich, Switzerland

<sup>3</sup> HYDRO Exploitation SA,  
Rue de l'Industrie 10, CH-1951, Sion, Switzerland

<sup>4</sup> Alpiq SA,  
Ch. de Mornex 10, CH-1003, Lausanne, Switzerland

## Abstract

Pelton turbines are known for their robustness and efficiency. Despite their reliability, challenges such as crack propagation and hydro-abrasive erosion persist, necessitating new condition monitoring strategies to enhance operational safety. This paper proposes a methodology for detecting, identifying, and classifying the natural frequencies of Pelton runners during startup transients to detect early-stage damages like erosion and cracks. The study focuses on the dynamic behaviour of Pelton turbines at the Vissoie hydraulic power plant, employing finite element method simulations, experimental modal analysis (EMA), transmissibility experiments, and automated startup transient recordings. Key findings include the successful classification of runner vibration modes, validation of numerical simulations through the EMA, and evaluation of vibration transmission to bearings. A startup transient analysis revealed distinct frequency bands corresponding to runner natural modes, demonstrating repeatability and offering insights for long-term monitoring.

## 1 Introduction

Pelton turbines are recognized as the most efficient and developed impulse turbines [1]. They operate under high head and low discharges, making them widely used in mountainous regions. At the turbine inlet, water is evenly distributed to all injectors through a manifold. The injector needles are adjusted to control the flow rate, creating high-velocity water jets that tangentially impinge the turbine runner at the level of the buckets, where hydraulic power is transformed into mechanical power [2]. Two prevalent Pelton turbine unit configurations exist: horizontal and vertical with reference to the shaft orientation. Horizontal configurations are most suitable for turbines with up to three injectors, whereas vertical configurations are more adapted for turbines with up to six injectors. Regardless of their proven reliability and advanced development, manufacturers and operators still face three challenges identified by Grein et al. in 1984 [3]: (i) crack propagation due to material fatigue, (ii) hydro-abrasive erosion, and (iii) the presence of larger objects (rocks, branches) in the water that can obstruct injectors or impact the runner.

Currently, non-destructive testing and visual inspections remain the most effective methods for evaluating the severity of turbine component damage. Both methods require production downtime and are scheduled based on a preventive maintenance philosophy. However, cracks propagation from incipient damage to complete failure follows an exponential pattern, making it difficult to predict even with shortened inspection intervals [5]. Similarly, without continuous sediment monitoring, assessing the impact of hydroabrasive erosion on

turbine components is challenging.

Previous studies have explored the feasibility of implementing a condition monitoring vibration-based approach for detecting early-stage damage in Pelton turbines [4][5]. Both studies focus on bucket failure cases that occurred due to crack propagation, leading to the detachment of a large portion of the bucket. Another study [6] found that during the early phase of a startup, natural frequencies matching those of the runner are noticeable on the bearings of two Pelton turbines. This suggests that the initial jet impacts may excite the runner's natural modes, similar to a hammer blow. Based on this hypothesis, high frequency vibration recording during the initial phase of a startup could allow the extraction of the runner's natural frequencies, enabling monitoring of their evolution in the presence of incipient damage (e.g., erosion, cracks).

Here, we propose a methodological approach for the detection, the identification, and the classification of the natural frequencies of Pelton runners during the early phase of startup transients. Most steps described in this methodology were previously presented in a study by Egusquiza [6]. The methodology aims to detect incipient damages that may develop in the Pelton runners by monitoring the unit's dynamic behavior through the bearings. Given the complexity of Pelton runners as cyclic structures, a deep understanding of their dynamic behavior is essential. Additionally, understanding how their dynamic behavior evolves in the presence of damage is crucial. However, this aspect is the focus of an ongoing study and will therefore not be presented herein.

## 2 Methods and materials

### 2.1 Test case and methodology

The Pelton turbines examined in this study are located at the Vissoie Hydraulic Power Plant (HPP), which is part of the Forces Motrices de la Gougra (FMG) hydroelectric scheme in Switzerland. The HPP is equipped with three identical power units, each with a capacity of 15 MW, featuring two Pelton turbines arranged in a horizontal configuration, as shown in Figure 1. The two Pelton turbines are positioned on either side of the generator in an almost symmetrical manner, with only the generator exciter disrupting the symmetry. Each Pelton turbine is fed by a single injector located at the lowest part of the turbine within the housing. The general characteristics of a Pelton turbine are provided in Table 1.

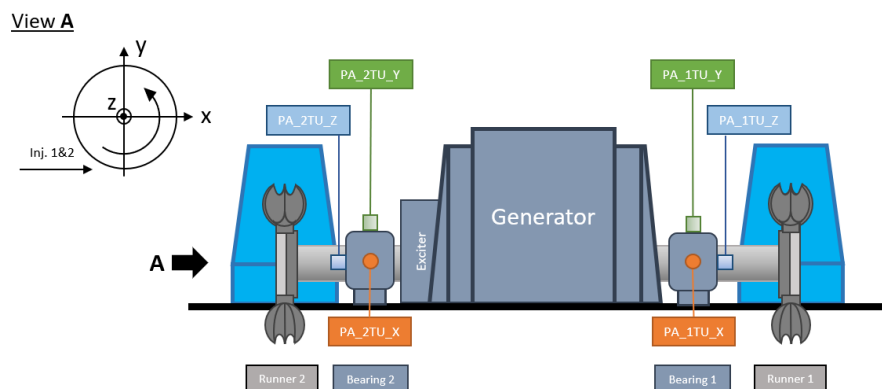


Figure 1: A power unit at the Vissoie HPP.

To enhance the condition monitoring of the existing Pelton units, the methodology detailed in Figure 2 was applied. The methodology is based on three approaches, each of which can be applied individually if needed. The first approach involves Finite Element Method (FEM) modal simulations of a runner to capture its vibration modes. The runner geometry was modeled using CAD software with the help of original drawings and 3D scans of the runner. After meshing the geometry, boundary conditions (BCs) were imposed to simulate either a free runner (free-BC) or a fixed runner (fixed-BC). The former allowed for calibration of the

Table 1: Main characteristics of one Pelton turbine at the Vissoie HPP. Each power unit at the Vissoie HPP is equipped with two Pelton turbines, one on each side of the generator.

Net Head	$H_n$	435	[ $m$ ]
Nominal discharge	$Q$	2	[ $m^3/s$ ]
Nominal output	$P$	7.5	[ $MW$ ]
Rotational speed	$n$	428	[ $min^{-1}$ ]
No. of buckets	$N$	21	[ $-$ ]
No. of injectors	$Z$	1	[ $-$ ]
Inner bucket width	$B$	502	[ $mm$ ]
Runner pitch diameter	$D_1$	1900	[ $mm$ ]
Specific speed (Pelton)	$N_s = D_1/B$	3.78	[ $-$ ]

simulation through comparison with an experimental modal analysis (EMA) performed on the standalone runner. The fixed-BC, on the other hand, was intended to replicate the BCs of the runner when mounted on the power unit. Once the vibration modes were captured both numerically and experimentally, a transmissibility experiment was conducted on-site with both runners mounted on the power unit. This experiment identifies the vibration modes that are transmitted to the bearing when the runner is impacted with an instrumented hammer. Finally, high-frequency accelerometer signals were automatically recorded during startup transients over several months. These signals were then extracted and post-processed offline. The present paper explores all the steps of this methodology, with a focus on the transmissibility experiment and the analysis of the startup transients.

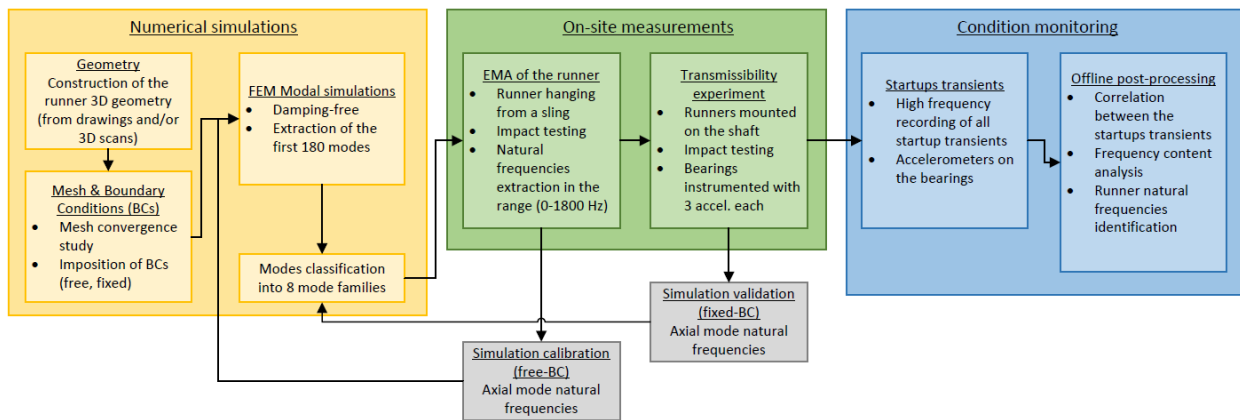


Figure 2: Methodology proposed to enhance the vibration-based condition monitoring of Pelton runners.

## 2.2 Numerical simulations

A Pelton runner displays a multitude of vibration modes across the frequency range of interest (0-1800 Hz), which complicates their differentiation. Therefore, FEM modal simulations were performed to aid in the classification of the runner modes. In addition, the simulations offer the possibility of testing different BCs and evaluate their influence on the vibration modes of the structure. The modal simulations were conducted using the commercial software Ansys Mechanical (2021 R2) and the numerical model workflow is depicted in Figure 3. The mesh was generated using the software's automatic mesher and consists of tetrahedral quadratic elements (Tetra10). The mesh comprises  $1.35 \cdot 10^6$  elements and  $2.00 \cdot 10^6$  nodes, with an element size of 15 mm. The mesh size was determined through a mesh convergence study to ensure the detection of all modes within the frequency range of interest. The first 180 vibration modes were extracted and classified into eight mode families, as already proposed in previous studies [6][7]: *Axial*, *Tangential*, *Tangential in*

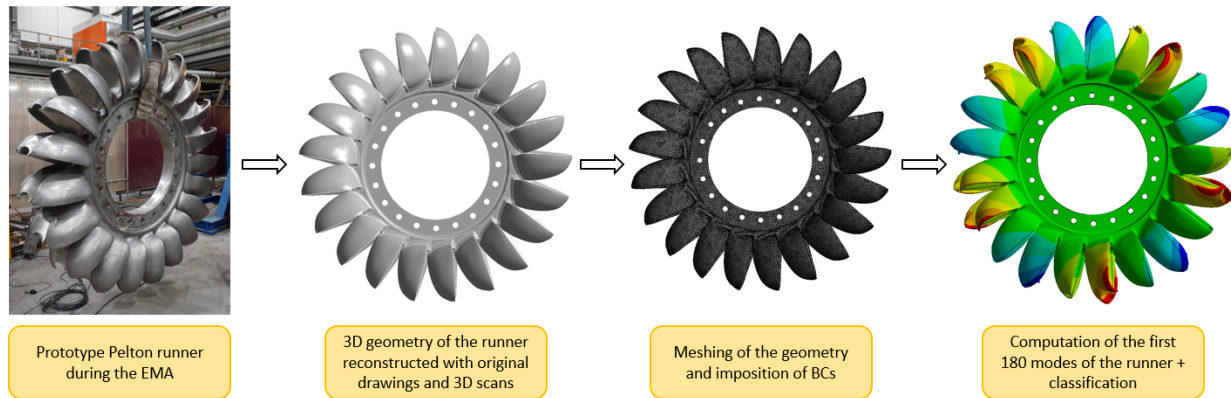


Figure 3: Numerical model workflow.

*counter-phase (c-ph.), Axial in c-ph., Radial in c-ph., Radial, Radial-axial in c-ph., and Radial-axial.* While these mode family names may vary in other studies [8][9], they represent the first eight families to appear in increasing frequency order.

## 2.3 On-site experiments

### 2.3.1 EMA of a free hanging runner

To validate the simulations, an EMA was performed on the runner dismantled from the power unit for maintenance purposes, allowing for the dynamic characterization of the runner alone. The left picture of Figure 3 shows the test conditions during the EMA, with the runner suspended by a sling positioned between two buckets. This boundary condition is expected to resemble the simulated free-BC, thereby allowing for simulation calibration. The experiment involved moving a tri-axis accelerometer across various measurement locations while the hammer impacted a fixed location. Given the complexity of the mode shapes, a large number of measurement locations are necessary to accurately identify and differentiate all modes. Despite the complex geometry of the buckets, and due to software limitations, the buckets were simplified to six measurement points each, with four points instrumented. Consequently, the experimental mode extraction did not allow for a satisfactory classification of the modes. To overcome this limitation, frequency response functions (FRFs), denoted  $H(\omega)$  in Equation 1, were primarily extracted from the EMA to detect the natural frequencies of the runner. In Equation 1,  $X(\omega)$  and  $F(\omega)$  represent the fast Fourier transform (FFT) coefficients of the output signal  $x(t)$  (accelerometer signal) and the input signal  $f(t)$  (impact hammer force signal), respectively. The natural frequencies were identified by peaks in the magnitude plot of several FRFs and then compared with the computed numerical natural frequencies.

$$H(\omega) = \frac{X(\omega)}{F(\omega)} \quad (1)$$

### 2.3.2 Transmissibility experiment

A transmissibility experiment was conducted on the power unit with both runner mounted on the shaft to evaluate the vibration transmission from the runners to the bearings. The experimental setup is presented in Figure 1. Three mono-axis accelerometers were mounted on each bearing:  $PA_{1TU}$  and  $PA_{2TU}$ . The accelerometers were oriented in the X, Y, and Z directions according to the coordinate system shown in the same figure. X and Y represent the radial-horizontal and radial-vertical directions, respectively, while Z represents the axial direction (Figure 1). In addition to these accelerometers, one accelerometer was placed on one bucket of each runner (bucket 16) in the axial direction (Z direction). Following a sensitivity analysis,

it was found that the axial direction serves as a privileged sensing location capable of detecting all vibration modes of a runner, even with a mono-axis accelerometer. This effectiveness is attributed to the significant involvement of the bucket side (rim) vibration in most mode shapes.

The experiment involves impacting the bucket adjacent to the one equipped with a mono-axis accelerometer. Per impact, eight FRFs are computed between the accelerometers and the hammer signals. As derived in [10], a local transmissibility function (TF) can be calculated as the ratio of the FFT coefficients  $X_l(\omega)$ ,  $X_m(\omega)$  of two output signals,  $x_l(t)$  and  $x_m(t)$ , where indexes  $l$  and  $m$  stand for sensing locations:

$$T_{lm}(\omega) = \frac{X_l(\omega)}{X_m(\omega)} \quad (2)$$

In the case of a the same input signal, Equation 3 can be derived from Equation 2, where  $F_j(\omega)$  stands for the FFT coefficients of the hammer force signal applied at location  $j$ .

$$T_{lm}(\omega) = \frac{H_{lj}(\omega)F_j(\omega)}{H_{mj}(\omega)F_j(\omega)} = \frac{H_{lj}(\omega)}{H_{mj}(\omega)} \quad (3)$$

Therefore, local TFs are computed as the ratio of FRFs which share the same input signal. Using this relationship, TFs were computed between each measurement position and the bucket measurement position, resulting in seven local TFs for a single impact. After performing the first impact on bucket 16 of runner 1, the process was repeated on bucket 16 of runner 2, enabling the computation of seven additional TFs.

## 2.4 Automated startup transients recording

Since July 2023, signals from five accelerometers (*PA\_1TU\_X*, *PA\_1TU\_Y*, *PA\_2TU\_X*, *PA\_2TU\_Y*, and *PA\_2TU\_Z*) have been automatically recorded and stored for all startup transients of the three power units of the HPP. The signal recording starts when the unit receives the startup order, and signals are recorded for the first 100 seconds of the startup. Data are collected as waveforms with a sampling frequency of 12.8 kHz, that are first stored locally and then exported for advanced post-processing.

## 3 Results

### 3.1 Runner modes and experimental validation

The names of the mode families originate from the observation of single bucket mode shapes. In the frequency band of interest, there are only eight bucket modes, but when considering the full runner, each bucket mode appears 21 times due to cyclic symmetry. These occurrences of the same mode family are classified according to the number of nodal diameters (NDs) associated to each mode. NDs are imaginary lines that cross the structure radially, indicating where a phase shift occurs in the mode shape. The maximal number of NDs,  $ND_k$ , is determined by the number of sectors (buckets)  $N$  in a cyclic structure, following the rule  $ND_k = N/2$  when  $N$  is even and  $ND_k = (N - 1)/2$  when  $N$  is odd. For the present runner,  $ND_k = 10$ , resulting in NDs ranging from  $ND_0$  to  $ND_{10}$  in increments of 1, as depicted in Figure 4. For all  $ND_i \geq ND_1$ , there exists a pair of modes, called "double modes," with similar natural frequencies but different mode shapes, as described in [11].

Each mode family exhibits an asymptotic pattern when reaching high NDs. However, some mode families spread over large frequency bands (*Axial*, *Radial in c-ph.*, *Radial-axial in c-ph.*), while others are concentrated within narrower frequency bands (*Tangential*, *Tangential in c-ph.*, *Axial in c-ph.*). The broad spread of the *Axial* mode family makes it the best candidate for calibrating numerical simulations, as the frequencies within this family are well separated from each other, making them easier to identify in a FRF.

The calibration procedure was performed by adjusting the mass-stiffness ratio of the material in the simulation through modifications to the material density and the Young's Modulus, respectively. The results of the

calibration are presented in Figure 5, where the simulated natural frequencies and are in very good agreement with the experimental ones.

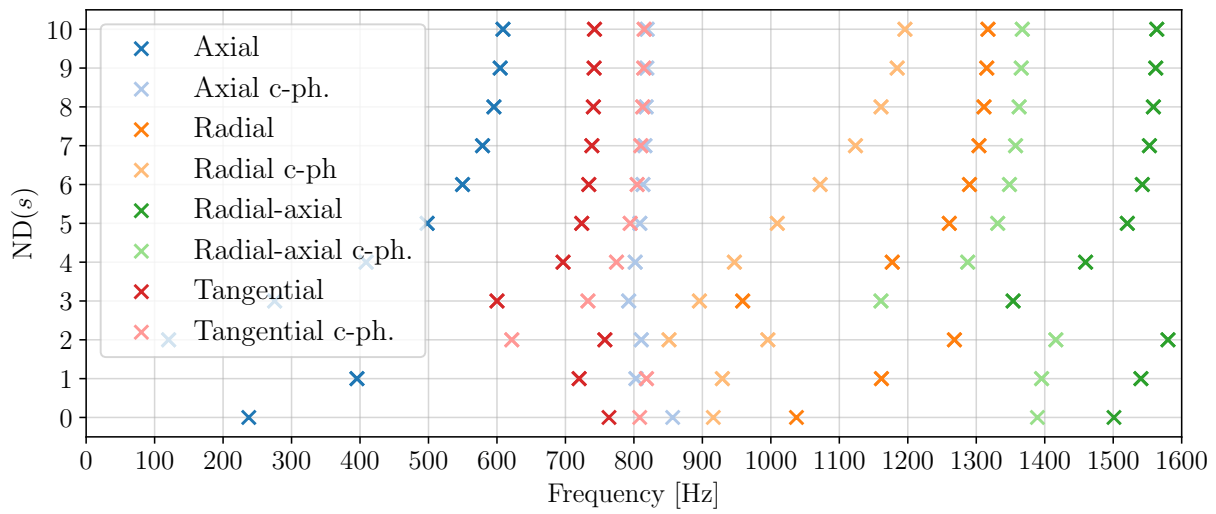


Figure 4: First eight runner mode families classified according to their natural frequencies and number of nodal diameters.

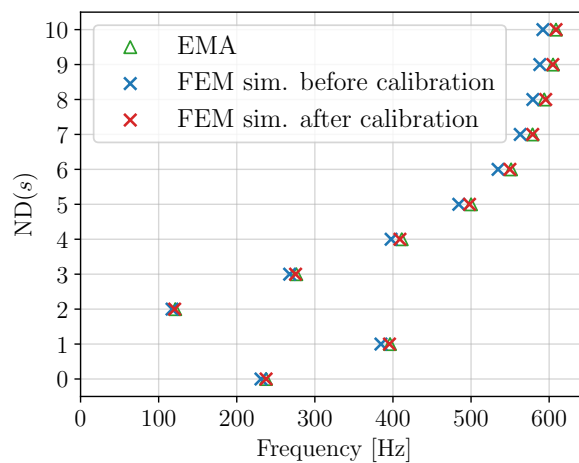


Figure 5: Results of the model calibration on the *Axial* mode family.

### 3.2 Transmissibility from the runners to the bearings

Figures 6 and 7 show the results of the transmissibility experiment conducted from runner 1 to bearing 1. Both figures present the same FRFs and TFs but cover different frequency intervals. The colored bands illustrate the spread of each mode family for the modes  $ND_4$  to  $ND_{10}$ . The top graphs display the FRFs, while the bottom graphs present the TFs, which are the ratios of the bearing FRFs to the runner FRF (reference FRF), as detailed in section 2.3.2.

The runner FRF allows for the identification of most natural frequencies of the runner. However, with a frequency resolution of  $0.625 \text{ Hz}$  for the FRF, some modes cannot be isolated, particularly in regions where

the mode density is high, such as the 720-850  $Hz$  frequency band, where three mode families overlap. Nevertheless, the FRFs measured from the bearing highlight the feasibility of capturing most natural frequencies of runner 1 from bearing 1. In the 720-850  $Hz$  frequency band, the *Tangential* and *Tangential in c-ph.* modes show the best transmissibility, as illustrated in Figure 6 by the close proximity of the FRFs in the top graph and the high level of the TFs in the lower graph. In Figure 7, the *Radial-axial* and *Radial-axial in c-ph.* mode families exhibit the best transmissibility for most of their natural frequencies in the 900-1800  $Hz$  frequency band. While antiresonances are well captured by the runner FRF, they are not as well represented in the bearing FRFs, leading to local peaks in the TFs. Therefore, computing transmissibility values only in the presence of a mode would be more representative than displaying TFs across the full frequency range.

In addition, the mean values of the TFs were computed over the entire frequency range of 0-1800  $Hz$  and are displayed in Table 2. These mean values represent the signal attenuation from each runner to the monitoring locations on the bearings. Generally, TFs exhibit higher mean values for the bearings adjacent to the impacted runner. However, in the case of impact on runner 1, the TF at location *PA\_2TU\_Z* shows a similar level to the mean TFs at bearing 1. Furthermore, the mean TFs indicate good reciprocity when impacting runner 1 and measuring at bearing 2, and vice versa, with all mean TFs falling within a range of 3.31-6.08 %. The highest mean TFs are observed from runner 2 to bearing 2. This could be attributed to a higher loading of bearing 2 due to the asymmetry introduced by the exciter on the side of bearing and runner 2. Finally, the mean TFs in the Z direction are consistently the highest among those for a given bearing, which is not surprising since the buckets of both runners were impacted axially during the experiment. Despite the discrepancies highlighted, all mean TFs lie within the range of 3.31 - 10.16 %, which does not clearly favor one sensing location over another.

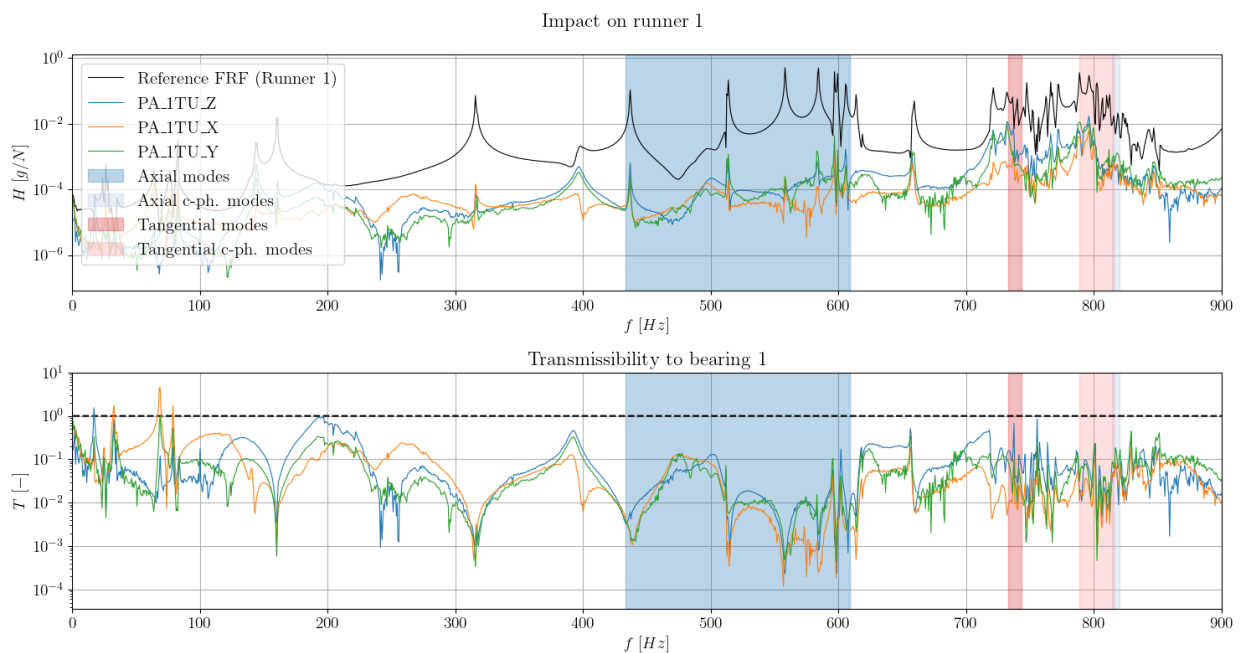


Figure 6: FRFs and local TFs computed on the 0-900  $Hz$  frequency interval from runner 1 to bearing 1. The colored frequency bands stand for the  $ND_4 - ND_{10}$  modes of each mode family.

### 3.3 Startup transients

The post-processing of the startup transients has revealed that sensing locations in the Y direction exhibit larger vibration amplitudes than those in X direction. Additionally, the frequency content of sensors placed in the Y direction aligns with the natural frequencies of the runners. Therefore, this section will focus on startup transients recorded by the accelerometer *PA\_1TU\_Y* of unit 2. Initially, pre-processing was conducted on all

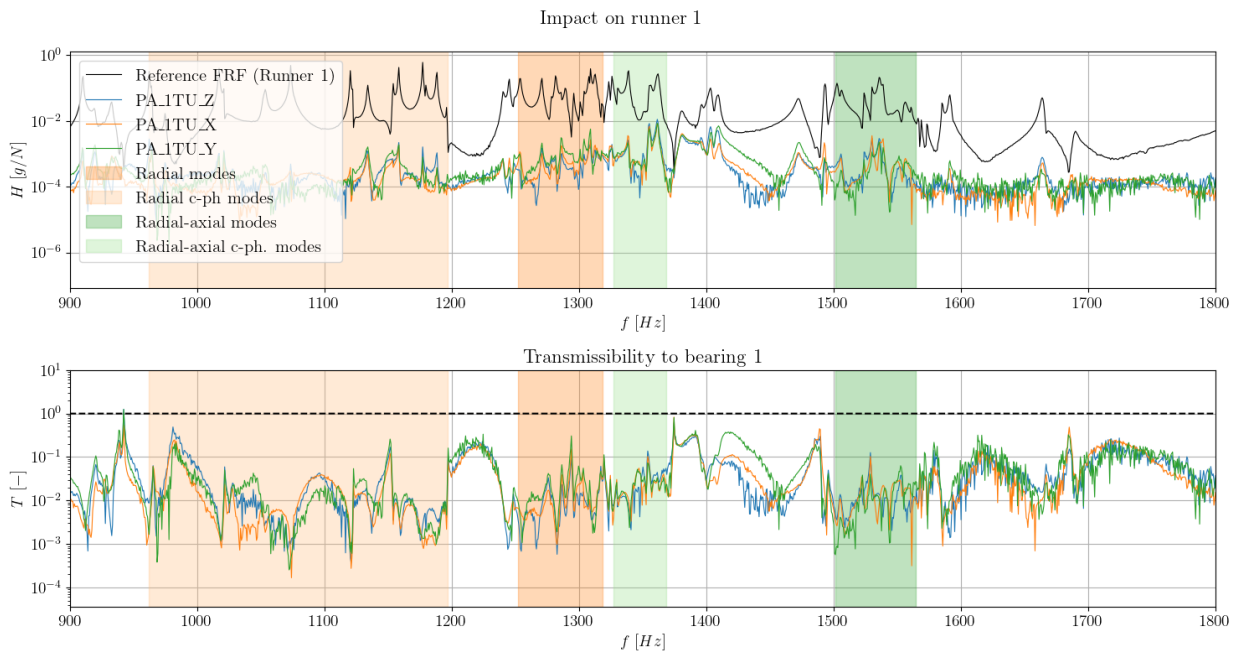


Figure 7: FRFs and local TFs computed on the 900-1800  $Hz$  frequency interval from runner 1 to bearing 1. The colored frequency bands stand for the  $ND_4 - ND_{10}$  modes of each mode family.

Table 2: Mean transmissibility  $\bar{T}$  for each sensor computed over the 0-1800  $Hz$  frequency band.

<i>Sensor</i>	$\bar{T}$ [%] (runner 1)	$\bar{T}$ [%] (runner 2)
<i>PA_1TU_X</i>	6.76	3.31
<i>PA_1TU_Y</i>	6.39	4.62
<i>PA_1TU_Z</i>	7.80	5.30
<i>PA_2TU_X</i>	4.24	6.52
<i>PA_2TU_Y</i>	5.25	9.17
<i>PA_2TU_Z</i>	6.08	10.16

startup recordings to exclude faulty acquisitions or incomplete startups. A total of 20 individual startups were retained for further analysis. The initial impact, defined as  $t_i$  was identified when the signal's standard deviation exceeded a given threshold. One second of data was retained before  $t_i$ , and all signals were trimmed to a maximum length of 60 seconds. Figure 8 shows the power spectrum of two startups recorded a month apart. The power spectrum  $S_{xx}$  was computed using a sliding Hamming window of 1 second with a window overlap of 0.5 second, resulting in a frequency resolution of  $\Delta f = 1 Hz$  and 121 slices for the time vector. The acceleration phase of the unit is clearly visible, marked by the bucket passing frequency (BPF) and its harmonics. The BPF is calculated as the number of buckets multiplied by the unit's rotation frequency. Here, at nominal speed, the BPF is 150  $Hz$ , which is reached after 35 seconds for both startups. In both power spectra, the highest frequency amplitudes are observed within the first 20 seconds of the startup, as indicated by the lower plots of Figure 8. During this period, the excited frequencies are not correlated with the rotating speed of the unit. This initial bursts visible in the time signals (upper plots) of Figure 8 are attributed to the high-velocity jets impacting the stationary runners to initiate rotation. It should be noted that the angular position of the runner at the beginning of the startup depends on the previous shutdown phase and is thus different for every startup. However, the two power spectra exhibit similar patterns and frequency content, indicating good reproducibility between the two startup transients despite their seemingly random nature.

To evaluate the repeatability between the startups, portions of the power spectra were selected to characterize their frequency content, and to calculate an ensemble average. Figure 9 shows the 20 startups, 5 seconds after

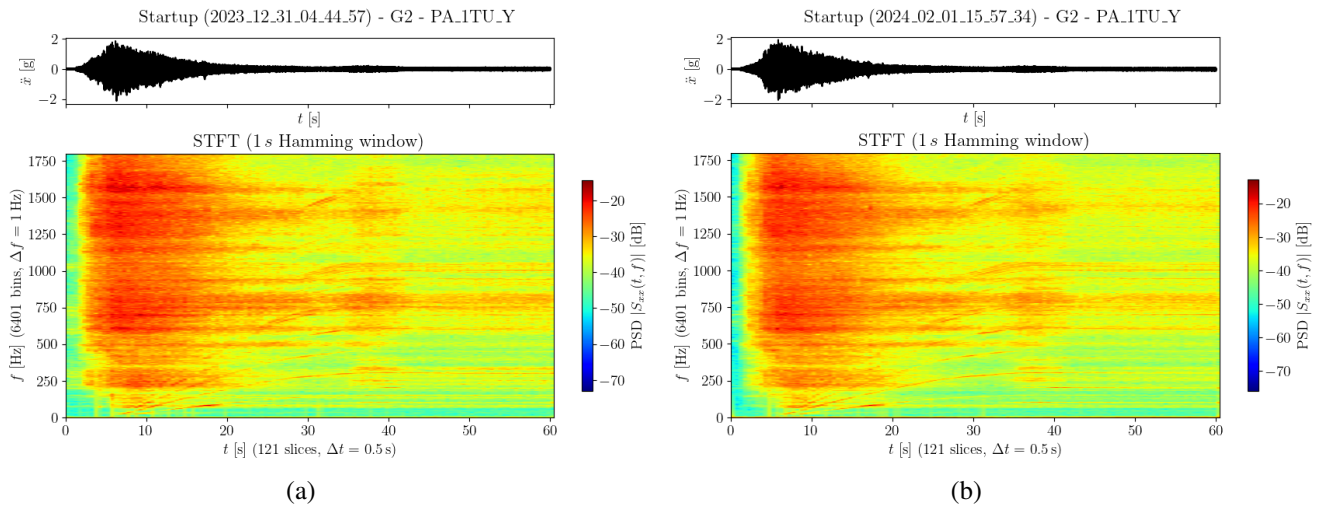


Figure 8: Power spectrum of two distinct startups recorded by the accelerometer *PA\_1TU\_Y* on unit 2.

$t_i$ , thus 6 seconds after the beginning of the signals. The graphs display three frequency bands, where the largest amplitudes are present within the spectrum and that match the natural frequencies of the runners. Figure 9a focuses on the 560 - 640 *Hz* band, related to the *Axial* modes. Figure 9b highlights the 650 - 850 *Hz* band, which includes a large number of runner modes, namely the *Tangential*, *Tangential in c-ph.*, and the *Axial in c-ph.* modes. Finally, the 1500 - 1700 *Hz* band is shown in Figure 9c, corresponding to the *Radial-axial* modes. Each blue curve represents a single startup, with darker curves indicating more recent startups and lighter curves representing older startups. Despite differences between the startups, with local peaks appearing at different frequencies, the ensemble average curves demonstrate clear repeatability, highlighting the trend of each frequency band.

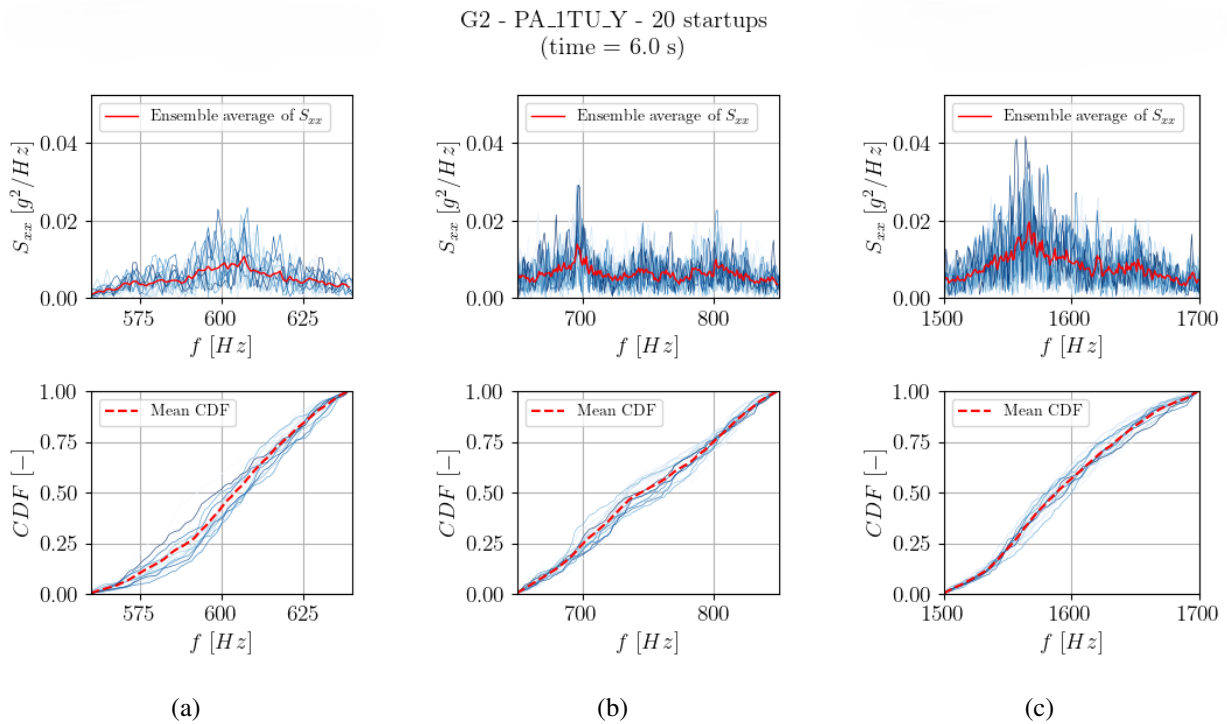


Figure 9:  $S_{xx}$  (top graphs) and normalized cumulative sum of 20 startups (bottom graphs) recorded on unit 2, five seconds after  $t_0$  for the frequency bands (a) 560-640 *Hz*, (b) 650-850 *Hz*, and (c) 1500-1700 *Hz*.

The ensemble average in Figure 9a shows a peak at 610 *Hz*, matching the natural frequency of the *Axial*

$ND_{10}$  mode. Conversely, a peak at nearly 700 Hz in Figure 9b does not align with any natural frequency of the runner, as indicated in Figure 6. The highest amplitudes in the power spectra are found in the 1500-1700 Hz frequency band, with a pronounced peak around 1560 Hz, corresponding to the natural frequencies of the high *ND Radial-axial* modes. Additionally, the cumulative sums for each frequency band are presented with their respective means shown as dashed red curves. Since each frequency band features a distinct signature, the cumulative sums could be useful for detecting long-term frequency-shift trends. Finally, it should be noted that enhancing the accuracy of the initial impact detection method could strengthen the trends presented in this study.

## 4 Conclusions

In this study, a comprehensive methodological approach was proposed and tested for the detection, identification, and classification of the natural frequencies of Pelton runners during the early phase of startup transients. The approach integrates FEM simulations, EMA, a on-site transmissibility experiments, an automatic high frequency data acquisition during the startups.

The results demonstrated that the vibration modes of the Pelton runner, identified through FEM simulations, align well with the experimental data. The transmissibility experiments revealed that most natural frequencies of the runner can be effectively captured from the bearing measurements, with certain mode families, such as the *Tangential* and *Radial-axial* modes, showing the highest transmissibility.

The analysis of the recorded startup transients highlighted the initial impact of the water jets as a critical phase for exciting the runner's natural frequencies, as already demonstrated in the literature. The power spectra of the startups showed distinct frequency bands corresponding to the *Axial*, *Tangential*, and *Radial-axial* modes. Despite some variations between individual startups, the ensemble average curves indicated clear repeatability, suggesting the potential for this method to monitor the dynamic behavior of the runner over time.

Finally, an onboard monitoring of the Pelton runners would be necessary in order to validate the startup transients frequency contents, and to investigate the source of the frequencies that could not be matched with any natural frequency of the runners (700 Hz e.g.).

## Acknowledgements

This work is part of the Hydro Alps Lab research activities. The authors would like to thank FMG and ALPIQ for their valuable contribution to this study by allowing privileged access to the Vissoie HPP. This study would not have been possible without the help of HYDRO Exploitation which provided valuable technical support throughout the study.

## References

- [1] E. Quaranta and C. Trivedi, "The state-of-art of design and research for Pelton turbine casing, weight estimation, counterpressure operation and scientific challenges," *Heliyon*, vol. 7, no. 12, p. e08527, dec 2021.
- [2] Z. Zhang, *Pelton Turbines*. Heidelberg: Springer International Publishing, 2016.
- [3] H. Grein, R. Angehrn, and M. Lorenz, "Inspection periods of Pelton runners," in *The 12th IAHR Symposium*, IAHR, Ed., vol. 1. Stirling: IAHR, Aug. 1984, pp. 421–444.
- [4] W. Zhao, M. Egusquiza, A. Estevez, A. Presas, C. Valero, D. Valentín, and E. Egusquiza, "Improved damage detection in Pelton turbines using optimized condition indicators and data-driven techniques," *Structural Health Monitoring*, vol. 20, no. 6, pp. 3239–3251, jan 2021.

- [5] M. Egusquiza, E. Egusquiza, C. Valero, A. Presas, D. Valentín, and M. Bossio, “Advanced condition monitoring of Pelton turbines,” *Measurement*, vol. 119, pp. 46–55, apr 2018.
- [6] M. Egusquiza, “Study of the dynamic behavior of Pelton turbines,” Ph.D. dissertation, Universitat Politècnica de Catalunya. Departament de Mecànica de Fluids, 2020.
- [7] M. Egusquiza, C. Valero, D. Valentín, A. Presas, and E. Egusquiza, “Dynamic response of Pelton runners: Numerical and experimental analysis in prototypes,” *Renewable Energy*, vol. 157, pp. 116–129, sep 2020.
- [8] J. Schmied, T. Weiss, R. Angehrn, D. JS, L. VA, T. HYDRO, L. VA, T. HYDRO, and Ltd., “Detuning of Pelton runners,” in *7th IFToMM-Conference on Rotor Dynamics, Vienna, Austria, 25-28 September 2006*, 2006.
- [9] M. Sick, W. Michler, T. Weiss, and H. Keck, “Recent developments in the dynamic analysis of water turbines,” *Proceedings of the Institution of Mechanical Engineers, Part A: Journal of Power and Energy*, vol. 223, no. 4, pp. 415–427, apr 2009.
- [10] W.-J. Yan, M.-Y. Zhao, Q. Sun, and W.-X. Ren, “Transmissibility-based system identification for structural health monitoring: Fundamentals, approaches, and applications,” *Mechanical Systems and Signal Processing*, vol. 117, pp. 453–482, Feb. 2019.
- [11] D. J. Ewins, “Vibration characteristics of bladed disc assemblies,” *Journal of Mechanical Engineering Science*, vol. 15, no. 3, pp. 165–186, Jun. 1973.